Decentralized Primary Frequency Regulation for Hybrid Multi-terminal Direct Current Power Systems Considering Multi-source Enhancement

Jialiang Wu, Zhen Wang, *Member*, *IEEE*, Ruixu Liu, Yu Shan, and Chenxuan Wang

***Abstract*—Hybrid multi-terminal direct current (MTDC) transmission technology has been a research focus, and primary frequency regulation (FR) improvement in the receiving-end system is one of the problems to be solved. This paper presents a decentralized primary FR scheme for hybrid MTDC power systems considering multi-source enhancement to help suppress frequency disturbance in receiving-end systems. All the converters only need local frequency or DC voltage signal input to respond to system disturbance without communication or a control center, i.e., a decentralized control scheme. The proposed scheme can activate appropriate power sources to assist in FR in various system disturbance severities with fine-designed thresholds, ensuring sufficient utilization of each power source. To better balance FR performance and FR resource participation, an evaluation index is proposed and the parameter optimization problem is further conducted. Finally, the validity of the proposed scheme is verified by simulations in MATLAB/Simulink.**

***Index Terms*—Decentralized control scheme, primary frequency regulation (FR), rate of change of frequency (ROCOF), system frequency disturbance.**

I. Introduction

NOWADAYS, climate change resulted from carbon emission has been of great concern all over the world. Wind power has rapidly developed in recent years and been of great importance in power supply. Wind farms (WFs) can be connected to the main grid via high-voltage direct current (HVDC) technology. On the one hand, line-commutated converter (LCC) based HVDC technology has the characteristics of large capacity and low power loss but large reactive compensation and commutation failure risk when operating as an inverter [1]. On the other hand, voltage-source converter (VSC) based HVDC technology can control active and reactive power independently and realize self-commutation but with high power loss and construction cost [2]. Compared with two-level VSC, modular multilevel converter (MMC) is more promising with higher output waveform quality and stronger fault handling capability, hence it is becoming more widely-used in engineering projects [3]. To combine and exert the merits of LCC- and MMC-HVDC in the aspects of technology and economy, hybrid HVDC has been proposed and applied in practice in recent years [4], [5]. For instance, the first hybrid multi-terminal direct current (MTDC) transmission system worldwide, Kunliulong DC project, has been put into operation in China, being an important scientific and technological innovation all over the world [5].

As for MTDC transmission system, there usually exist several measures for enhancing frequency performance in the receiving-end system, and this paper mainly focuses on primary frequency regulation (FR). Some researchers focus on the distributed energy resources in the receiving-end system to assist in FR, the representative of which is battery energy storage system (BESS). It possesses fast dynamic response and high output precision and can effectively reduce the frequency deviation [6]. A common control strategy for BESSs is called synthetic inertia control, combining the conventional droop control with inertia emulation function to govern the power output and improve the system frequency response [7]. Besides, a two-layer control scheme with a modified droop control is proposed in [8], enhancing the robustness of the controller and dynamic stability of the system. Reference [9] tries to coordinate multiple distributed BESSs with online optimization to provide cost-effective frequency support, and a fuzzy controller is designed in [10] to smooth the power of the BESS and extend its lifetime. Nevertheless, since the power output of the BESS is limited, it may require coordination of other power sources when a large system disturbance occurs. Besides, the state of charge (SOC) of BESS should also be concerned during the operation to avoid the over-charging/over-discharging of the BESS.

An alternative of FR control strategy is to make other HVDC-interconnected systems provide primary FR support. Some researchers utilize communication among converters to transmit frequency signal so that other networks can assist in FR. A control strategy for a point-to-point HVDC link feeding into a low-inertia AC grid is proposed in [11]. It us-

Manuscript received: January 12, 2023; revised: March 8, 2023; accepted: March 23, 2023. Date of CrossCheck: March 23, 2023. Date of online publication: May 4, 2023.

This work was supported by the National Natural Science Foundation of China (No. 52077196) and the Science and Technology Project of State Grid Zhejiang Electric Power Co., Ltd. (No. 5211JY21N001).

J. Wu, Z. Wang (corresponding author), R. Liu, Y. Shan, and C. Wang are with the College of Electrical Engineering, Zhejiang University, Hangzhou 310027, China, and C. Wang is also with the Economic Research Institute of State Grid Zhejiang Electric Power Co., Ltd., Hangzhou 310016, China (e-mail: 11810035@zju.edu.cn; eezwang@ieee.org; lrx19970408@zju.edu.cn; yshan@zju.edu.cn; wang_chenxuan@zj.sgcc.com.cn).

DOI: 10.35833/MPCE.2023.000017

es the angular aperture between the phase angle of the sending-end system voltage and the phase-shifting angle of the rectifier to regulate the power flow, hence assisting in FR for the receiving-end grid. Some researchers propose a novel frequency controller for the sending-end WF in [12], adopting synthetic control in under-frequency range and droop control in over-frequency range. However, the necessity of information exchange with communication in the above strategies reduces system operation reliability [13]. To address this problem, [14] demonstrates a communication-free FR control strategy, which can adjust DC voltage according to system frequency fluctuation. Thus, artificial coupling between interconnected networks is established and the frequency information can be detected by measuring local DC voltage. This strategy is further improved and adopted in two- and multi-terminal systems, coordinating HVDC-interconnected sending-end AC systems and WFs to participate in FR [15]-[18]. Though the problem of communication is solved, the still existing drawback of these methods is that AC systems and WFs participate in FR as soon as frequency disturbance takes place even if the disturbance is small, hence frequently affecting their operation states and the system operation economy.

Based on the above analysis, this paper proposes a decentralized primary FR control scheme for hybrid MTDC power systems, which coordinates multiple power sources, i.e., sending-end AC system, WF, and local BESS, to participate in primary FR in receiving-end system. Different power sources are activated according to the system disturbance severity, and all the controllers need to detect local signals without a control center. In this way, the frequency disturbance in receiving-end systems can be suppressed by sufficiently utilizing the FR capability of each power source. Meanwhile, wind turbine generator (WTG) in WF can operate in the maximum power point tracking (MPPT) mode normally and in the droop mode as needed to balance the operation economy and FR requirement.

The main contributions of this paper can be listed as follows.

1) A decentralized primary FR control scheme for hybrid MTDC power systems is proposed, wherein all the converters only need to input local frequency or DC voltage signal to respond to system disturbance without communication or a control center.

2) A logistic function based power limitation coefficient for the BESS is introduced, which can correct the power output of the BESS according to its operating mode and SOC to avoid its over-charging/over-discharging and extend its service life.

3) The coordination of multiple power sources can be achieved with fine-designed thresholds for the converter controllers. Hence, the appropriate power sources can be selected to participate in FR according to system disturbance severity, so that the system stability can be maintained with less frequent FR participation and the wind energy utilization can be increased.

The rest of this paper is organized as follows. Section II demonstrates the system configuration and the existing problem in the conventional FR control scheme. Section III introduces the proposed control scheme (PCS) in detail from the aspects of the overall design and the controller improvement. The tuning of the key parameters, including threshold values and droop coefficients, is conducted in Section IV. Section V provides the simulation results. Finally, discussions and conclusions are presented in Sections VI and VII, respectively.

II. System Configuration and Problem Description

A. System Configuration

In Fig. 1, a hybrid MTDC system considering wind power transmission is used for FR study, and it can cover several application scenarios such as VSC-HVDC systems with WF connection [15], LCC-HVDC systems [19], and hybrid LCC-MMC systems [20], which will be further discussed in Section VI. In Fig. 1, for the sake of simplicity, two synchronous generators (SGs) are used to represent the sending-end system AC2 and the receiving-end system AC1, respectively. A single doubly-fed induction generator (DFIG) based WTG is used to represent the whole aggregated WF. The two AC systems and the WF are interconnected via three HVDC converters: REMMC, SELCC, and WFMMC. The power from the two sending ends AC2 and WF is transmitted to the receiving-end system AC1 through a hybrid HVDC system. To enhance FR, a BESS station near REMMC is connected to AC1 via BAMMC. The arrows in Fig. 1 denote the positive power flow direction.

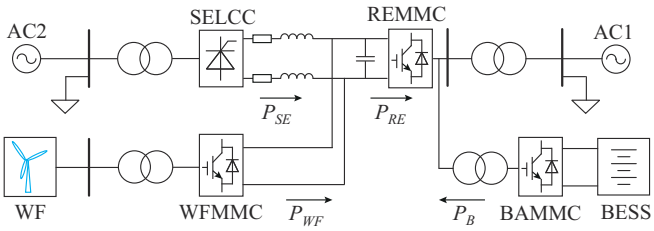

Fig. 1. Diagram of studied hybrid MTDC system.

B. Conventional Control Scheme (CCS)

In CCS, when disturbance occurs in AC1, the possible FR strategies for converters in Fig. 1 are as follows.

1) BAMMC synthetic inertia control. The BESS power output reference P_B^* changes with frequency deviation as follows [7]:

$$P_B^* = P_{B0} - K_{Bi}F_{RE} - K_{Bd}\Delta f_{RE} \tag{1}$$

where Δf_{RE} is the frequency deviation in AC1, and $F_{RE} = \mathrm{d}\Delta f_{RE}/\mathrm{d}t$ is the corresponding rate of change of frequency (ROCOF); P_{B0} is the initial power reference under normal condition and is generally set to be 0; and K_{Bi} and K_{Bd} are the inertial and droop coefficients for BAMMC, respectively.

2) REMMC DC voltage droop control. The DC voltage reference $U_{dc,RE}^*$ changes with frequency deviation as follows [15]:

$$U_{dc,RE}^* = U_{dc0,RE} + K_U\Delta f_{RE} \tag{2}$$

where $U_{dc0,RE}$ is the rated DC voltage; and K_U is the droop coefficient for REMMC.

In this way, the frequency deviation is converted into DC voltage deviation, and interconnected networks can receive frequency variation in AC1 by detecting DC voltage fluctuation without communication.

3) SELCC active power droop control. With U_{dc}-P droop control, the power reference P_{SE}^{*} changes as follows:

$$P_{SE}^{*}=P_{SE0}-K_P\Delta U_{dc,SE} \tag{3}$$

where P_{SE0} is the initial power reference; $\Delta U_{dc,SE}$ is the measured DC voltage deviation; and K_P is the SELCC droop coefficient.

4) WFMMC frequency droop control. With U_{dc}-f droop control, WF frequency reference f_{WF}^{*} changes as follows [15]:

$$f_{WF}^{*}=f_{WF0}+K_f\Delta U_{dc,WF} \tag{4}$$

where f_{WF0} is the rated WF frequency; $\Delta U_{dc,WF}$ is the measured DC voltage deviation; and K_f is the WFMMC droop coefficient.

5) WF active power droop control. With f-P droop control, the WF power output reference P_{WF}^{*} changes as follows [15]:

$$P_{WF}^{*}=P_{WF0}-K_\sigma\Delta f_{WF} \tag{5}$$

where P_{WF0} is the initial WTG power output, generally determined by MPPT control mode; Δf_{WF} is the WF frequency deviation; and K_σ is the droop coefficient for WF.

Therefore, given the droop control rules in (1)-(5), when frequency of AC1 changes, the primary FR can be improved with the coordination of the BESS, AC2, and WF: ① the BESS detects the frequency deviation directly and can absorb or release energy in response to frequency fluctuation; and ② the DC voltage will change with frequency deviation simultaneously, and AC2 and WF are enabled to adjust power output to participate in FR by measuring local DC voltage variation.

Such a control scheme can improve the frequency response and suppress the frequency disturbance of the receiving-end system. However, the main problem of the above control scheme is that all the power sources participate in FR simultaneously once frequency disturbance occurs even if the disturbance is small. In this way, the normal operation of AC2 and WF may be frequently affected, reducing system operation economy. Besides, the BESS power output is not limited when the SOC is too high or too low, which may result in over-charging and over-discharging of the BESS and affect its lifetime.

III. Proposed Decentralized Primary FR Control Scheme

To avoid the aforementioned problems, a decentralized primary FR control scheme is proposed in this paper. The diagram of the overall PCS is illustrated in Fig. 2, in which different power source controls can participate in FR according to the system disturbance severity: ① the BESS converter control; ② the receiving-end converter control; and ③ the WF converter control. In addition, the sending-end converter SELCC and the WF in Fig. 2 will also participate in FR and use the conventional control rules in Section II, and the determination of the droop coefficients K_P and K_σ will be further discussed in Section IV.

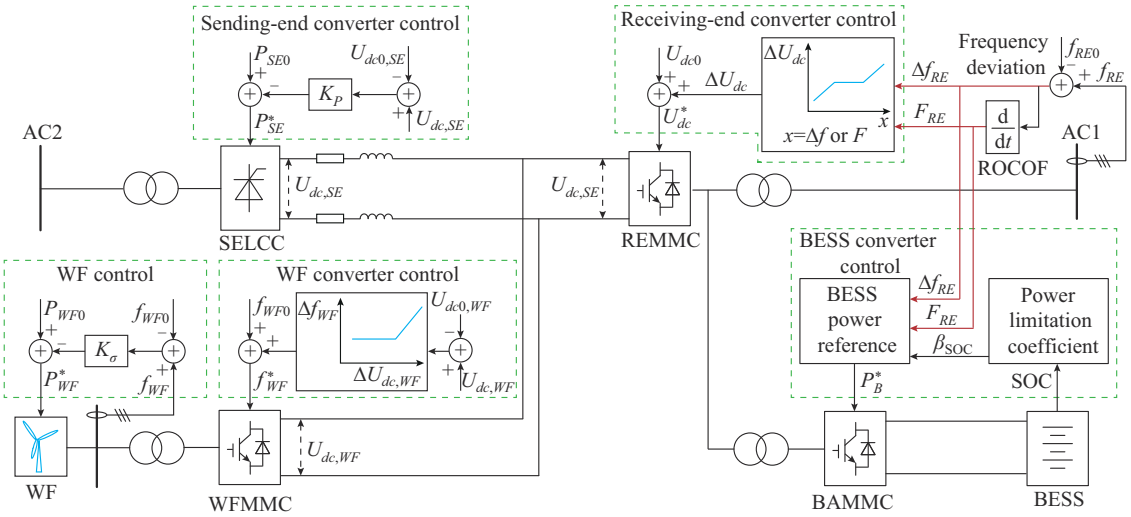

Fig. 2. Diagram of overall PCS.

The control input signals in Fig. 2 include two types: ① frequency deviation and ROCOF for REMMC and BESS; and ② DC voltage signal for SELCC and WFMMC.

A. BESS Converter Control

The BESS converter BAMMC starts to participate in FR whenever load variation occurs in the receiving-end system. In order to avoid the over-charging and over-discharging of the BESS and extend its service life, the BESS power will be further corrected. The BESS power reference in Fig. 2 is designed as:

$$P_B^{*}=\beta_{\mathrm{SOC}}\left(P_{B0}+\Delta P_B^{*}\right) \tag{6}$$

$$\Delta P_B^{*}=-K_{Bi}F_{RE}-K_{Bd}\Delta f_{RE} \tag{7}$$

where ΔP_B^{*} is the increment of BESS power reference; and β_{SOC} is the power limitation coefficient, related to BESS operating mode and the SOC. Equation (6) shows that the BESS charging/discharging power should be limited when

the SOC is close to its limited value. The details of β_{SOC} is explained below.

Generally, the SOC of BESS can be divided into three zones for two operating modes, respectively, as illustrated in Fig. 3.

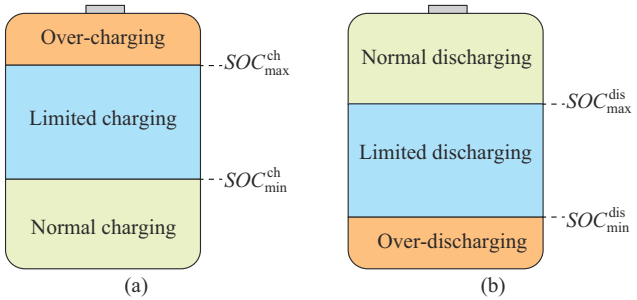

Fig. 3. SOC partition diagram of BESS for charging mode and discharging mode. (a) Charging mode. (b) Discharging mode.

1) Charging mode: ① normal charging, ② limited charging, and ③ over-charging, with typical boundary values SOC^{ch}_{max}=90%, SOC^{ch}_{min}=40% [10].

2) Discharging mode: ① normal discharging, ② limited discharging, and ③ over-discharging, with typical boundary values SOC^{dis}_{max}=60%, SOC^{dis}_{min}=10% [10].

The BESS power limitations in each zone are different. Taking the charging mode for instance (the discharging case is similar), in normal charging zone, BESS can absorb energy with high power and little limitation; in limited charging zone, the charging power needs to decrease rapidly with the increasing SOC to avoid over-growth of SOC value; in over-charging zone, BESS stops charging for extending battery lifetime.

To realize such BESS charging/discharging performance, a logistic function is introduced to calculate β_{SOC} as:

$$\beta_{SOC}=\begin{cases}\dfrac{e^{-k(SOC-SOC^{ch})}}{1+e^{-k(SOC-SOC^{ch})}} & \text{charging mode}\\ \dfrac{e^{k(SOC-SOC^{dis})}}{1+e^{k(SOC-SOC^{dis})}} & \text{discharging mode}\end{cases} \tag{8}$$

where SOC is the SOC value of the BESS; $SOC^{ch}=(SOC^{ch}_{max}+SOC^{ch}_{min})/2$; $SOC^{dis}=(SOC^{dis}_{max}+SOC^{dis}_{min})/2$; and k is a coefficient to determine the steepness of the curves, as illustrated in Fig. 4. In this way, β_{SOC} is a kind of common symmetric "S" fitted function, which can well fulfill the above charging/discharging characteristics. The relationship between β_{SOC} and SOC for the charging mode can be described as follows. The value of β_{SOC} is close to 1 as SOC increases when $SOC<SOC^{ch}_{min}$; then β_{SOC} decreases rapidly and is close to 0; when $SOC>SOC^{ch}_{max}$, $\beta_{SOC}\approx 0$. The similar conclusion can be drawn for the discharging mode.

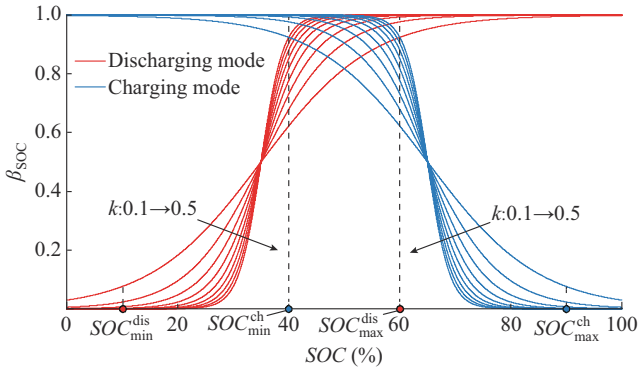

Fig. 4. Curves of β_{SOC} with different values of k.

B. Receiving-end Converter Control

The receiving-end converter REMMC is activated to transfer frequency information into DC voltage for FR when the disturbance in the receiving-end system increases and the ROCOF or frequency deviation exceeds their threshold values μ_F and μ_{fd}, i.e., $|F_{RE}|>\mu_F$ or $|\Delta f_{RE}|>\mu_{fd}$. The corresponding control rule is designed as:

$$U^*_{dc,RE}=U_{dc0,RE}+\Delta U^*_{dc1,RE}+\Delta U^*_{dc2,RE} \tag{9}$$

$$\Delta U^*_{dc1,RE}=\begin{cases}K_{Ui}(F_{RE}-\text{sign}(F_{RE})\cdot\mu_F) & |F_{RE}|>\mu_F\\ 0 & |F_{RE}|\le\mu_F\end{cases} \tag{10}$$

$$\Delta U^*_{dc2,RE}=\begin{cases}K_{Ud}(\Delta f_{RE}-\text{sign}(\Delta f_{RE})\cdot\mu_{fd}) & |\Delta f_{RE}|>\mu_{fd}\\ 0 & |\Delta f_{RE}|\le\mu_{fd}\end{cases} \tag{11}$$

where K_{Ui} and K_{Ud} are the DC voltage droop coefficients; sign(·) denotes the sign of ROCOF and frequency deviation; and $\Delta U^*_{dc1,RE}$ and $\Delta U^*_{dc2,RE}$ represent the inertial term and the droop term, respectively, as shown in Fig. 5(a) and (b), where F_{max}, Δf_{max}, and ΔU_{dcmax} are the maximum allowed ROCOF, frequency deviation, and DC voltage deviation, respectively. The dead-band set in (10) and (11) corresponds to the REMMC activation requirement, i.e., the thresholds μ_F and μ_{fd} determine when to activate REMMC for FR, and the details of how to set these thresholds will be explained in Section IV.

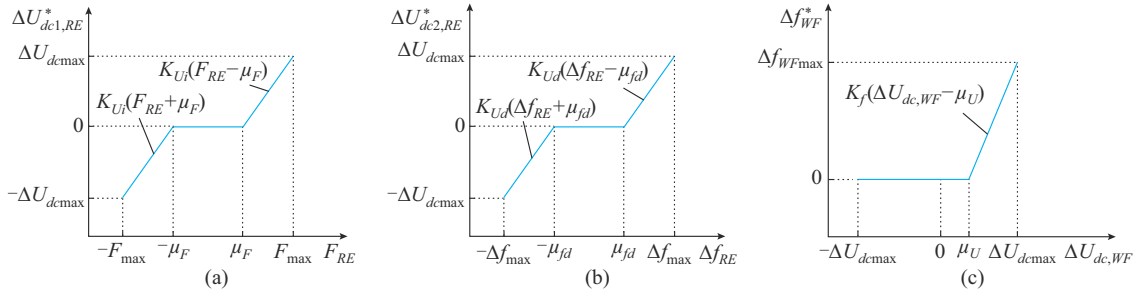

Fig. 5. Curves of $\Delta U^*_{dc1,RE}$ with respect to F_{RE}, $\Delta U^*_{dc2,RE}$ with respect to Δf_{RE}, and Δf^*_{WF} with respect to $\Delta U_{dc,WF}$. (a) $\Delta U^*_{dc1,RE}$ with respect to F_{RE}. (b) $\Delta U^*_{dc2,RE}$ with respect to Δf_{RE}. (c) Δf^*_{WF} with respect to $\Delta U_{dc,WF}$.

C. WF Converter Control

The WF converter WFMMC is activated to increase the WF frequency when the large load decrease occurs and the local DC voltage deviation exceeds its threshold value μ_U with the increase of ROCOF and frequency deviation in the receiving-end system, i. e., $\Delta U_{dc,WF} > \mu_U$. The control rule is designed as:

$$f_{WF}^{*} = f_{WF0} + \Delta f_{WF}^{*} \tag{12}$$

$$\Delta f_{WF}^{*} = \begin{cases} K_f(\Delta U_{dc,WF} - \mu_U) & \Delta U_{dc,WF} > \mu_U \\ 0 & \Delta U_{dc,WF} \le \mu_U \end{cases} \tag{13}$$

where Δf_{WF}^{*} represents the droop term, as shown in Fig. 5(c), where $\Delta f_{WF\max}$ is the maximum frequency deviation of the normal operating range of WTG. Similarly, the dead-band set in (13) corresponds to the WFMMC activation requirement, i. e., the threshold μ_U determines when to activate WFMMC for FR, and the details of how to set the threshold will also be explained in Section IV.

It should be noted that the WF frequency can only be increased and the reason is explained as follows. WTG operates in MPPT mode under normal condition, and theoretically, it can further increase or decrease its power output for FR with droop control in (5). However, under the situation of power increase, a second frequency dip may occur during the recovery of WTG speed. Since it is not the key point of this paper, we assume that the WTG can only reduce the power output for FR and, according to (5), the WF frequency can only be increased in large load decrease scenario.

D. Discussion

Based on the aforementioned analysis, different power sources are activated according to the receiving-end system disturbance severity, as summarized in Table I.

TABLE I
PROPOSED POWER SOURCE ACTIVATION SCHEME

Local signal characteristic	Source activated for FR or not			Application scenario
	BESS ($\lvert F_{RE}\rvert \ne 0$ or $\lvert \Delta f_{RE}\rvert \ne 0$)	Sending-end AC system ($\Delta U_{dc,SE} \ne 0$)	WF and WFMMC ($\Delta U_{dc,WF} > \mu_U$)	
1) $\lvert F_{RE}\rvert \le \mu_F$ and $\lvert \Delta f_{RE}\rvert \le \mu_{fd}$ 2) $\Delta U_{dc,SE} = 0$ 3) $\Delta U_{dc,WF} = 0$	√	×	×	Small load variation
1) $\lvert F_{RE}\rvert > \mu_F$ or $\lvert \Delta f_{RE}\rvert > \mu_{fd}$ 2) $\Delta U_{dc,SE} \ne 0$ 3) $\Delta U_{dc,WF} \le \mu_U$	√	√	×	Medium load variation or large load increase
1) $\lvert F_{RE}\rvert > \mu_F$ or $\lvert \Delta f_{RE}\rvert > \mu_{fd}$ 2) $\Delta U_{dc,SE} \ne 0$ 3) $\Delta U_{dc,WF} > \mu_U$	√	√	√	Large load decrease

It can be observed from Table I that:

1) When both the ROCOF and frequency deviation are within the threshold values, i. e., $|F_{RE}| \le \mu_F$ and $|\Delta f_{RE}| \le \mu_{fd}$, which corresponds to small load variation scenario, the DC voltage is maintained rated according to (10) and (11), thus the local DC voltage deviation values in SELCC and WFMMC are zero, i.e., $\Delta U_{dc,SE} = 0$ and $\Delta U_{dc,WF} = 0$.

In this scenario, only the local BESS in the receiving-end system is firstly utilized to suppress the disturbance with (7), while the sending-end AC system and WF are not activated.

2) With the increase of system disturbances such as medium load variation or large load increase, either of ROCOF and frequency deviation exceeds the threshold values, i. e., $|F_{RE}| > \mu_F$ or $|\Delta f_{RE}| > \mu_{fd}$. According to (10) and (11), REMMC starts to change DC voltage so that both SELCC and WFMMC detect the DC voltage deviation, which, however, may be within the threshold value of WFMMC, i. e., $\Delta U_{dc,SE} \ne 0$ and $\Delta U_{dc,WF} \le \mu_U$.

In this scenario, the sending-end AC system also participates in FR jointly with the BESS according to (3). The WF frequency remains rated according to (13), hence the WTG remains to operate in MPPT mode.

3) Different from the above two scenarios, there also exists a situation that the DC voltage deviation measured in WFMMC increases to exceed the threshold value, i. e., $\Delta U_{dc,WF} > \mu_U$. Such situation may happen when large load decrease occurs.

In this scenario, the BESS and sending-end AC system participate in FR, the WFMMC is also activated to increase WF frequency according to (13), and the WF assists in FR with (5).

In conclusion, the local measured signals will vary when system disturbance scenario changes, and the power sources are activated for FR only when specific activation criteria are satisfied.

The PCS has the following features.

1) All the converters only need to input local frequency or DC voltage signal to participate in FR without control center or extra communication, i.e., a fully decentralized control.

2) With specific thresholds, different power sources can be activated to assist in FR in various system disturbance severities. In this way, local sources are used in priority while AC2 and WF will participate in FR only when specific criteria are satisfied, and WTG can operate in MPPT in most scenarios. Hence, the FR capability of each power source can be sufficiently utilized and the operation economy of WF can be adequately considered.

3) Compared with the CCS, an additional term is added to reflect ROCOF when calculating the DC voltage reference. In this way, sending-end systems and WF can also provide certain inertia support to suppress ROCOF.

IV. PARAMETER DESIGN BASED ON OPTIMIZATION

There are two main aspects that should be taken into consideration in parameter design: on the one hand, the performance of control scheme is our main focus to obtain the optimal control parameters; on the other hand, the system stability should also be ensured under the obtained parameters.

A. Key Designed Parameters

1) BESS Power Limitation Coefficient

The determination of k in (8) is introduced as follows. According to β_{SOC} characteristics, it is assumed that when SOC=

SOC^{ch}_{max}, the value of β_{SOC} is close to zero (e.g., 10^{-3} in this paper), hence the BESS stops charging in the over-charging zone. Then, it is easily obtained that $k=0.28$. The same result can be obtained for the discharging mode considering symmetry.

2) Threshold Values

In order to sufficiently utilize the FR capability of BESS, it is considered that when either of F_{RE} and Δf_{RE} reaches μ_F and μ_{fd}, the BESS power output also reaches the maximum. Hence, combining (6) and (7), μ_F and μ_{fd} can be set as:

$$\mu_F=\Delta P_{B\max}/(\beta_{SOC}K_{Bi})=P_{B\max 0}/K_{Bi} \tag{14}$$

$$\mu_{fd}=\Delta P_{B\max}/(\beta_{SOC}K_{Bd})=P_{B\max 0}/K_{Bd} \tag{15}$$

where $\Delta P_{B\max}=\beta_{SOC}P_{B\max 0}$ is the maximum power variation of BESS; and $P_{B\max 0}$ is the nominal maximum power of BESS.

Similarly, it is considered that when $\Delta U_{dc,WF}$ reaches μ_U, the power output variation of sending-end system is also maximized, and the DC voltage deviation in SELCC at this time is denoted as $\mu_{U,SE}$. To establish the relationship between $\mu_{U,SE}$ and μ_U, it is assumed that the DC voltage deviation at all nodes are identical since the cable resistance is generally small and can be neglected [21]. Thus, combining (3), μ_U can be set as:

$$\mu_U=\mu_{U,SE}=\Delta P_{SE\max}/K_P \tag{16}$$

where $\Delta P_{SE\max}=\eta P_{res}$ is the maximum power output variation of the sending-end system, and P_{res} and η are the total power reserve of the sending-end system and the ratio for supporting other interconnected systems, respectively.

Equations (14)-(16) define all the three threshold values. Once given the maximum power reserves of BESS and sending-end system and the droop coefficients K_{Bi}, K_{Bd}, and K_P, the threshold values can be fixed. The determination of K_{Bi}, K_{Bd}, and K_P will be introduced in the following.

3) Droop Coefficients

In receiving-end converter control, DC voltage needs to reach the maximum when either of F_{RE} and Δf_{RE} reaches the corresponding maximum allowed value, as illustrated in Fig. 5(a) and (b), respectively. Hence, combining (10) and (11), there are following constraints for droop coefficients K_{Ui} and K_{Ud}:

$$K_{Ui}=\Delta U_{dc\max}/(F_{\max}-\mu_F) \tag{17}$$

$$K_{Ud}=\Delta U_{dc\max}/(\Delta f_{\max}-\mu_{fd}) \tag{18}$$

where $F_{\max}$, $\Delta f_{\max}$, and $\Delta U_{dc\max}$ can be set to be 1 Hz/s, 0.5 Hz, and 0.1 p.u., respectively [22], [23].

As for WF converter control, WF frequency needs to reach the limitation value when the DC voltage deviation reaches the maximum, as illustrated in Fig. 5(c), while as for WF control, the power reduction of WTG also reaches the maximum at this moment. Hence, combining (5) and (13), the following constraints can be obtained for K_f and K_σ:

$$K_f=\Delta f_{WF\max}/(\Delta U_{dc\max}-\mu_U) \tag{19}$$

$$K_\sigma=\Delta P_{WF\max}/\Delta f_{WF\max} \tag{20}$$

where $\Delta P_{WF\max}=\sigma_{\max}P_{WF0}$ is the maximum power output variation of WF, and $\sigma_{\max}$ is the maximum power reduction ratio, generally set to be 0.2; and $\Delta f_{WF\max}$ can be set to be 0.5 Hz [24]. It is noted that these coefficients are not related to the control parameters inside WTG but only related to the maximum power reduction.

4) Parameter Optimization

In this paper, two types of measurement are considered for methodology evaluation: ① FR performance, including the maximum and steady-state frequency deviation, $|\Delta f_m|$ and $|\Delta f_s|$, respectively, and the maximum ROCOF $|F_m|$; ② FR resource participation, including the average power variation of BESS, AC2, and WF, denoted as $|\Delta\bar{P}_B|$, $|\Delta\bar{P}_{SE}|$, and $|\Delta\bar{P}_{WF}|$, respectively. Both types of measurement are expected to be as small as possible so that the system disturbance can be well suppressed and FR resources are utilized less frequently.

Hence, to evaluate both FR performance and FR resource participation, we first define an index M as:

$$M=M_f+M_P \tag{21}$$

$$M_f=c_{f1}|\Delta f_m|/\Delta f_{\max}+c_{f2}|\Delta f_s|/\Delta f_{\max}+c_{f3}|F_m|/F_{\max} \tag{22}$$

$$M_P=c_{P1}|\Delta\bar{P}_B|/\Delta P_{B\max}+c_{P2}|\Delta\bar{P}_{SE}|/\Delta P_{SE\max}+c_{P3}|\Delta\bar{P}_{WF}|/\Delta P_{WF\max} \tag{23}$$

where c_{f1}, c_{f2}, c_{f3}, c_{P1}, c_{P2}, and c_{P3} are the weight coefficients; and the form of $|X|/X_{\max}$ means the ratio of the measured value to the corresponding maximum allowed value, thus FR performance and FR resource participation are converted into the same dimension and then characterized by M_f and M_P, respectively.

As previously analyzed, the BESS, AC2, and WF are activated in different levels of system disturbance, and their activation thresholds and power output are directly determined by K_{Bi}, K_{Bd}, and K_P. Therefore, we need to comprehensively consider the evaluation indices of the system under a certain disturbance set, and then determine the value of the droop coefficients. In this paper, the disturbance set is designated as 5% to 45% load variations with interval of 10% so that different levels of system disturbance are considered.

Thus, the following optimization model is developed:

$$\min_{K_{Bi},K_{Bd},K_P}\sum_{i\in DS}M_i \tag{24}$$

s.t.

$$\begin{cases}\boldsymbol{x}(n+1)=\boldsymbol{A}\boldsymbol{x}(n)+\boldsymbol{B}\boldsymbol{u}(n)+\boldsymbol{R}\boldsymbol{r}(n)\\ \boldsymbol{y}(n)=\boldsymbol{C}\boldsymbol{x}(n)\end{cases} \tag{25}$$

$$K_{Bi\min}\le K_{Bi}\le K_{Bi\max} \tag{26}$$

$$K_{Bd\min}\le K_{Bd}\le K_{Bd\max} \tag{27}$$

$$K_{P\min}\le K_P\le K_{P\max} \tag{28}$$

where DS is the designed disturbance set; M_i is the evaluation index calculated by (21)-(23) under the system disturbance i; and $K_{Bi\min}$, $K_{Bi\max}$, $K_{Bd\min}$, $K_{Bd\max}$, $K_{P\min}$, and $K_{P\max}$ are the lower and upper bounds of K_{Bi}, K_{Bd}, and K_P, respectively. Equation (25) is the system state-space equation, which will be derived in Appendix A. Based on (14)-(16), it should be satisfied that $K_{Bi\min}=\Delta P_{B\max 0}/\mu_F$, $K_{Bd\min}=\Delta P_{B\max 0}/\mu_{fd}$, and $K_{P\min}=\Delta P_{SE\max}/\mu_U$, and the upper bounds of K_{Bi}, K_{Bd}, and K_P are set to be 10 times of their corresponding lower bounds to avoid system instability, which will be further demonstrat-

ed in the next subsection.

It can be observed from (24)-(28) that the parameter design problem is transformed into an optimization problem considering FR performance and FR resource participation. To solve the above parametric optimization problem, the particle swarm optimization (PSO) algorithm is employed in this paper, as it possesses advantages like speedy convergence and easy implementation, and it has been widely used to solve such problems in electrical engineering [25]. The parameters can be obtained by off-line optimization and are constant during the system operation once determined.

B. System Small-signal Stability

1) System Modeling and Validation

The detailed state-space model of the studied system in Fig. 1, including the dynamics of three MMC stations, one LCC station, DC network and their control system, and the detailed dynamic equations, can be found in [26]. Considering that this paper focuses more on FR and its control strategy, the detailed dynamics of converter, filter, and power sources can be simplified as first-order process [27], [28]. Thus, the system frequency response model (FRM) is shown in Fig. 6.

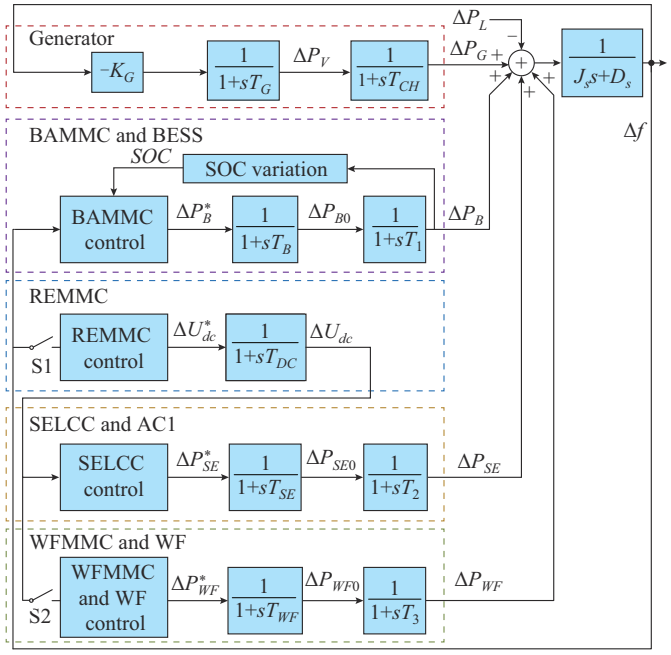

Fig. 6. System FRM.

In Fig. 6, s is the Laplace operator; ΔP_L is the load disturbance; ΔP_V is the governor position increment; ΔP_G is the power output variation of the SG; ΔP_{B0}, ΔP_{SE0}, and ΔP_{WF0} are the power responses to the power reference variations ΔP_B^*, ΔP_{SE}^*, and ΔP_{WF}^* of the BESS, AC1, and WF, respectively; ΔP_B, ΔP_{SE}, and ΔP_{WF} are the power responses of corresponding converters BAMMC, SELCC, and WFMMC, respectively; Δf is the frequency deviation; and ΔU_{dc} and ΔU_{dc}^* are the DC voltage deviation and its reference value, respectively. The physical meanings of the other parameters can be found in Appendix B Table BI and Table BII. The control blocks are corresponding to the control rules in Fig. 2.

There are two switches S1 and S2 in Fig. 6, representing the dead-band blocks in Fig. 2. The status of each switch changes according to local signals automatically in various scenarios in Table I, hence leading to three kinds of equivalent transfer functions of FRM: ① during small load variation period, both the switches S1 and S2 are open and only the BESS provides additional frequency support; ② in medium load variation or large load increase scenarios, with the switch S1 closed and S2 open, DC voltage starts to change and AC2 participates in FR; and ③ when large load decrease occurs, the switch S2 turns closed and WF further assists in FR.

In order to validate the accuracy of the proposed FRM, a comparison between the time-domain responses of the FRM and the detailed electrical model of the system in Fig. 1 is obtained in MATLAB/Simulink. The system parameters are given in Appendix B Table BI and Table BII. Figure 7 shows the system response to a successive load decrease in AC1 of 5%, 20%, and 20% at the time of 2 s, 8 s, and 14 s, respectively. Acceptable agreement between the results of the FRM and the detailed electrical model verifies the accuracy of the FRM.

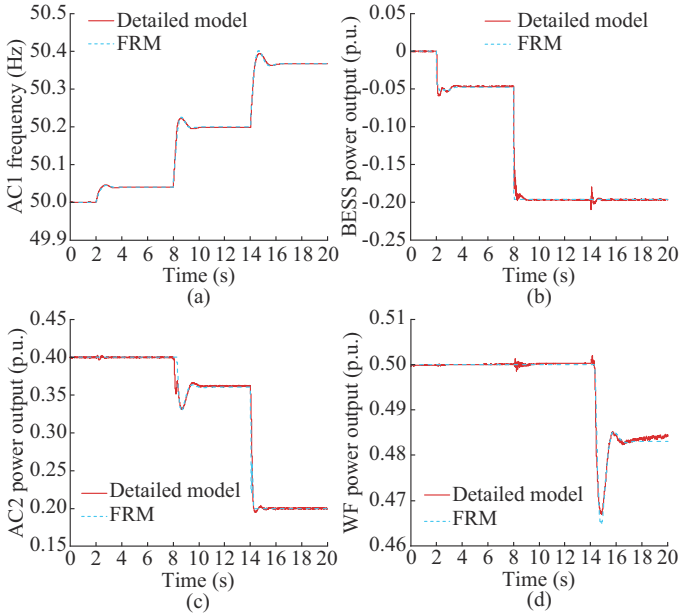

Fig. 7. System frequency response comparison during successive load decrease. (a) AC1 frequency. (b) BESS power output. (c) AC2 power output. (d) WF power output.

2) Analysis of Parameter Impact on System Small-signal Stability

The proposed FRM is used here for the analysis of the parameter impact on system small-signal stability. According to the previous parameter design, the threshold values and other droop coefficients are related to the droop coefficients K_{Bi}, K_{Bd}, and K_P, so the small-signal stability is conducted with the varying K_{Bi}, K_{Bd}, and K_P.

The dominant eigenvalue loci of the system with varying K_{Bi}, K_{Bd}, and K_P are given in Fig. 8, and it can be observed that the system eigenvalues may move to the right half plane if K_{Bi}, K_{Bd}, and K_P are too large and lead to system instability. Therefore, the maximum values of K_{Bi}, K_{Bd}, and K_P are

limited not to exceed 10 times of their corresponding minimum values to guarantee the system stability, which is consistent with the constraints in the optimization model.

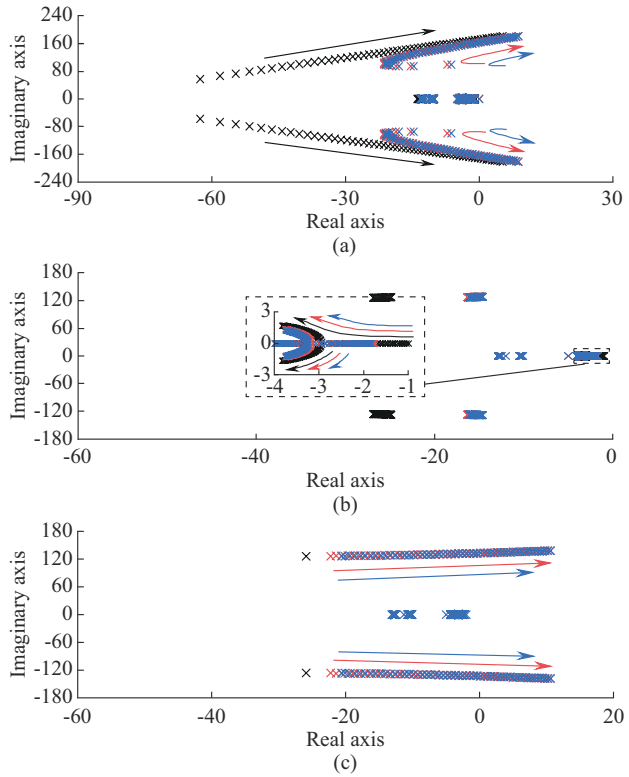

Fig. 8. Dominant eigenvalue loci of system with varying K_{Bi}, K_{Bd}, and K_P. (a) K_{Bi} varies from 1 to 30. (b) K_{Bd} varies from 2 to 40. (c) K_P varies from 2 to 30.

V. Case Study

To verify the effectiveness of the PCS, the simulation based on MATLAB/Simulink is carried out with the studied hybrid MTDC system depicted in Fig. 1. A comparison study is conducted between two schemes: ① the CCS in Section II; and ② the PCS in Section III. Based on the parameter design described in Section IV, it can be computed that $K_{Bi}=10.00$, $K_{Bd}=9.03$, and $K_P=4.57$ by solving the optimization problem with weight coefficients in Appendix B Table BIII, and other control parameters can be further calculated, as shown in Table II. The system parameters can be found in Appendix B Tables BI and BIV-BVI.

TABLE II
Control Parameters of Converters

Symbol	Item	Value
K_{Bi}, K_{Bd}	BAMMC power droop coefficients	10.00, 9.03
K_{Ui}, K_{Ud}	REMMC voltage droop coefficients	0.11, 0.26
K_P	SELCC power droop coefficient	4.57
K_f	WFMMC frequency droop coefficient	8.89
K_σ	WF power droop coefficient	0.40
μ_F	Threshold value of ROCOF	0.100 Hz/s
μ_{fd}	Threshold value of frequency deviation	0.110 Hz
μ_U	Threshold value of DC voltage deviation	0.044 p.u.

A. Case 1: Successive Load Variation

Under successive load variation events in AC1, as shown in Table III, the system response results of different control schemes are shown in Fig. 9.

TABLE III
Load Variation Events

Time (s)	Load variation event	Time (s)	Load variation event
6	Increase by 10%	24	Decrease by 25%
12	Increase by 15%	30	Decrease by 20%
18	Decrease by 30%		

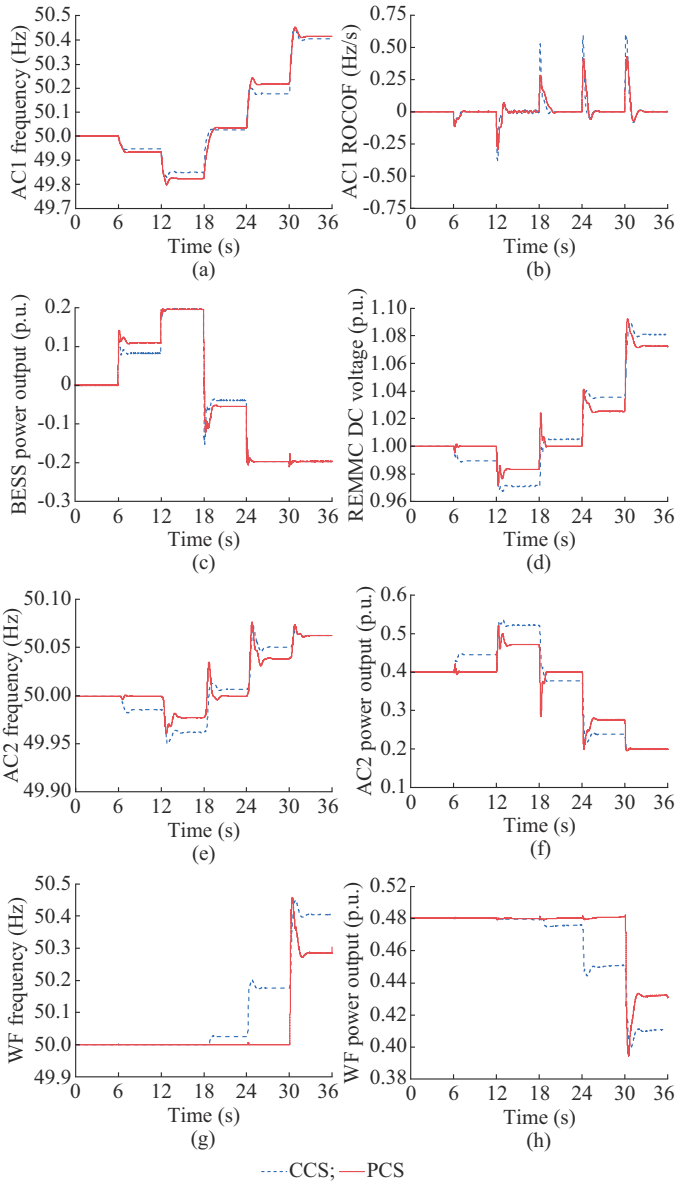

Fig. 9. System response results for successive load variation events in AC1. (a) AC1 frequency. (b) AC1 ROCOF. (c) BESS power output. (d) REMMC DC voltage. (e) AC2 frequency. (f) AC2 power output. (g) WF frequency. (h) WF power output.

The FR performance of AC1 is shown in Fig. 9(a) and (b). It can be observed that the frequency deviation suppression in CCS is slightly better than that in PCS when all the

power sources are considered to participate in FR simultaneously in CCS. Besides, since DC voltage transmits additional ROCOF information in PCS, the ROCOF of AC1 in PCS is more effectively limited than that in CCS.

Figure 9 illustrates the coordination of FR resources. It can be observed that in PCS, local BESS is utilized in priority, then AC2 assists in FR when the BESS power output reaches the maximum, and WF further participates in FR when AC2 power output also reaches the maximum. In this way, AC2 and WF can assist in FR less frequently and maintain normal operation as long as possible, and their frequency deviations are also smaller than those in CCS.

In order to further demonstrate the effectiveness and advantages of PCS, all the measurement values and evaluation index M in (21) for load variation events are listed in Table IV. It can be obviously observed that, the index M of PCS under any load variation event is smaller than that of CCS, i. e., PCS is better than CCS comprehensively considering FR performance and FR resource participation.

TABLE IV
MEASUREMENT VALUES AND EVALUATION INDEX FOR LOAD VARIATION EVENTS

Load variation event	Control scheme	FR performance			FR resource participation			Index M
		$\lvert\Delta f_m\rvert$ (Hz)	$\lvert\Delta f_s\rvert$ (Hz)	$\lvert F_m\rvert$ (Hz/s)	$\lvert\Delta\bar{P}_B\rvert$ (p.u.)	$\lvert\Delta\bar{P}_{SE}\rvert$ (p.u.)	$\lvert\Delta\bar{P}_{WF}\rvert$ (p.u.)	
Increase by 10%	CCS	0.057	0.044	0.123	0.086	0.037	0.000	1.424
	PCS	0.069	0.054	0.118	0.105	0.000	0.000	1.412
Increase by 15%	CCS	0.172	0.137	0.378	0.181	0.109	0.000	1.970
	PCS	0.202	0.159	0.297	0.184	0.063	0.000	1.794
Decrease by 30%	CCS	0.029	0.007	0.528	0.020	0.004	0.004	2.333
	PCS	0.036	0.012	0.284	0.038	0.006	0.000	1.765
Decrease by 25%	CCS	0.200	0.154	0.592	0.174	0.140	0.026	2.801
	PCS	0.242	0.185	0.413	0.176	0.110	0.000	2.033
Decrease by 20%	CCS	0.448	0.369	0.606	0.197	0.194	0.064	3.393
	PCS	0.453	0.382	0.429	0.197	0.188	0.047	2.773

B. Case 2: Influence of BESS Power Limitation Coefficient

In order to demonstrate the effect of the power limitation coefficient β_{SOC} on the BESS, a comparison study of BESS response curves with the same successive load variation events in Table III is illustrated in Fig. 10, wherein three groups of initial SOC values (SOC_0=30%, 50%, and 70%) are considered; and w/β and w/oβ denote that the β_{SOC} in (6) is adjustable as (8) and constant to be 1, respectively.

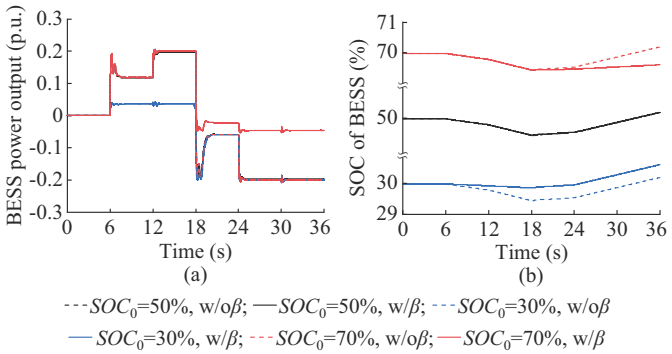

Fig. 10. BESS response curves considering charging/discharging limitation. (a) BESS power output. (b) SOC of BESS.

It can be observed from Fig. 10 that, given the rule in (8), the BESS power output can be effectively controlled with the variation of SOC. When the SOC is about 50%, β_{SOC} is close to 1 and the BESS power output is strictly limited. However, when the SOC increases to about 70% or decreases to about 30% as this case, β_{SOC} in charging/discharging mode reduces. Thus, the BESS power output and the growth/decline rate of the SOC can be limited, hence avoiding over-charging/over-discharging and extending the BESS service life.

C. Case 3: Successive System Faults

Under successive system fault events in AC and DC systems, as shown in Table V, the system response results of different control schemes are shown in Fig. 11.

TABLE V
SYSTEM FAULT EVENTS

Time (s)	Event
6	Three-phase grounding fault in AC1 for 0.05 s
12	10% SG tripping off in AC1
18	Wind speed variation from 12 m/s to 10 m/s
24	Disconnection of SELCC with the DC system

It can be observed from Fig. 11(a), during the fault events in Table V, PCS can still utilize FR resources to support FR for AC1. In particular, when three-phase grounding fault occurs, the system experiences a sharp frequency drop and can achieve fast and smooth recovery with PCS. Different from other events, after t=24 s, the frequency of AC1 in both CCS and PCS reaches the same value in Fig. 11(a). This is because in both schemes, the BESS power output reaches the maximum as shown in Fig. 11(b) and WF cannot provide more frequency support as shown in Fig. 11(d), i.e., the additional FR support from FR resources has reached the maximum. Such scenario may also happen when extremely large load variation occurs. In conclusion, PCS can provide sufficient FR support under fault conditions.

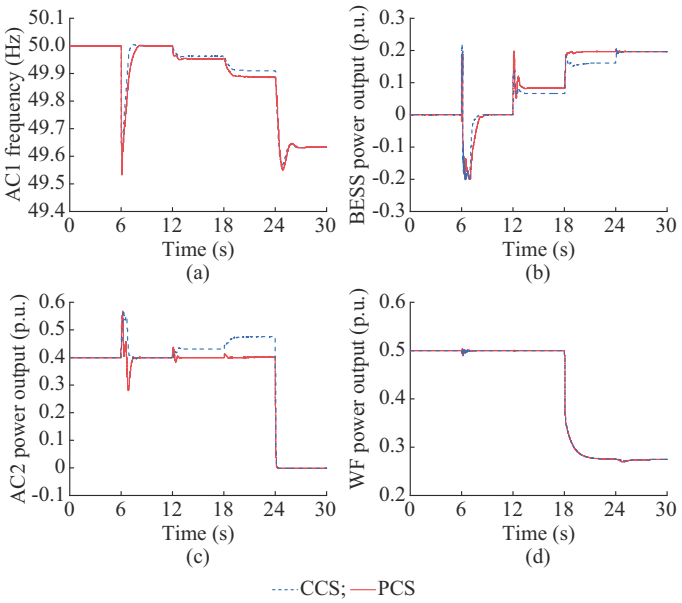

Fig. 11. System response results for successive system fault evernts in AC and DC systems. (a) AC1 frequency. (b) BESS power output. (c) AC2 power output. (d) WF power output.

VI. Discussion

In this paper, PCS is demonstrated via the studied system in Fig. 1; nevertheless, it is not designed only for the specific system topology. In fact, since the core of PCS is to make full use of ROCOF, frequency deviation, and DC voltage signals to reflect and transmit the system disturbance severity, and to activate appropriate power sources to assist in FR with fine-designed activation thresholds, PCS can also be applied in the following typical application scenarios.

1) The receiving-end inverter is also LCC, i.e., a full LCC-HVDC system. In this scenario, since the LCC inverter still adopts DC voltage control, it can also transmit frequency information to the sending-end system via DC voltage variation, i.e., PCS can be applicable.

2) The sending-end rectifier is also MMC, i. e., a full MMC-HVDC system. In this scenario, the MMC rectifier can still receive frequency information by detecting local DC voltage signal and then control its active power output, hence PCS can still be applicable.

3) More than one AC system and WF are interconnected, i. e., an MTDC system. In this scenario, DC voltage thresholds of each system and WF for activation can be designed with the same method introduced in Section IV. Therefore, PCS can also be applied in this scenario.

Therefore, it can be seen that the studied system in this paper is only one application scenario of PCS, and PCS can be further generalized to different scenarios in the future.

VII. Conclusion

In this paper, a decentralized primary FR control scheme for hybrid MTDC power systems considering multi-source enhancement is proposed. The PCS makes full use of ROCOF, frequency deviation, and DC voltage signals to reflect the system disturbance severity, and corresponding activation thresholds are designed for each power source to participate in primary FR. Specifically, when the BESS power output reaches the maximum, the sending-end AC system starts to assist in FR; and when the sending-end AC system also reaches the maximum power output, WF will be then activated. In other words, the PCS guarantees that the latter FR resource will be activated only when the former FR resource has reached its maximum power output. Thus, all the FR resources can less frequently participate in FR and be sufficiently utilized once activated. Such control scheme and parameter design approach can be adopted in other systems, and the generalized control scheme will be studied in our future work. Meanwhile, the power limitation coefficient for the BESS can effectively avoid its over-charging/over-discharging and extend its lifetime, which can be further applied on BESS operation in the future.

Appendix A

The state-space model of the FRM in Fig. 6 is derived here.

According to the control rules in (10), (11), and (13), the system state-space model will change and certain coefficients in the equations should be updated depending on the values of Δf, F, and ΔU_{dc}, and there are several situations, which are: ① $x>\mu_x$; ② $-\mu_x\le x\le\mu_x$; and ③ $x<-\mu_x$. x represents Δf, F, and ΔU_{dc}; and μ_x represents the corresponding threshold value. Therefore, the linearized discrete state-space equations can be derived as:

$$\Delta f(n+1)=\left(1-\frac{D_s T}{J_s}\right)\Delta f(n)+\frac{T}{J_s}(\Delta P_G(n)+\Delta P_B(n)+\Delta P_{SE}(n)+\Delta P_{WF}(n)-\Delta P_L(n)) \tag{A1}$$

$$F(n+1)=-\frac{D_s}{J_s}\Delta f(n)+\frac{1}{J_s}(\Delta P_G(n)+\Delta P_B(n)+\Delta P_{SE}(n)+\Delta P_{WF}(n)-\Delta P_L(n)) \tag{A2}$$

$$\Delta P_V(n+1)=-\frac{TK_G}{T_G}\Delta f(n)+\left(1-\frac{T}{T_G}\right)\Delta P_V(n) \tag{A3}$$

$$\Delta P_G(n+1)=\frac{T}{T_{CH}}\Delta P_V(n)+\left(1-\frac{T}{T_{CH}}\right)\Delta P_G(n) \tag{A4}$$

$$\Delta P_{B0}(n+1)=-\frac{TK_{Bd}}{T_B}\beta^*_{\mathrm{SOC}}\Delta f(n)-\frac{TK_{Bi}}{T_B}\beta^*_{\mathrm{SOC}}F(n)+\left(1-\frac{T}{T_B}\right)\Delta P_{B0}(n)-\frac{T}{T_B}\gamma^*\cdot SOC(n)+\frac{T}{T_B}\gamma^*\cdot SOC^* \tag{A5}$$

$$\Delta P_B(n+1)=\frac{T}{T_1}\Delta P_{B0}(n)+\left(1-\frac{T}{T_1}\right)\Delta P_B(n) \tag{A6}$$

$$SOC(n+1)=-\frac{T}{E_B}\Delta P_B(n)+SOC(n) \tag{A7}$$

$$\Delta U_{dc}(n+1)=a_1\Delta f(n)+a_2F(n)+\left(1-\frac{T}{T_{DC}}\right)\Delta U_{dc}(n)+b_1\mu_{fd}+b_2\mu_F \tag{A8}$$

$$\Delta P_{SE0}(n+1)=-\frac{TK_P}{T_{SE}}\Delta U_{dc}(n)+\left(1-\frac{T}{T_{SE}}\right)\Delta P_{SE0}(n) \tag{A9}$$

$$\Delta P_{SE}(n+1)=\frac{T}{T_2}\Delta P_{SE0}(n)+\left(1-\frac{T}{T_2}\right)\Delta P_{SE}(n) \quad \text{(A10)}$$

$$\Delta P_{WF0}(n+1)=a_3\Delta U_{dc}(n)+\left(1-\frac{T}{T_{WF}}\right)\Delta P_{WF0}(n)+b_3\mu_U \quad \text{(A11)}$$

$$\Delta P_{WF}(n+1)=\frac{T}{T_3}\Delta P_{WF0}(n)+\left(1-\frac{T}{T_3}\right)\Delta P_{WF}(n) \quad \text{(A12)}$$

where n is the sampling step; T is the sampling horizon; Δf^*, F^*, and SOC^* are the values of Δf, F, and SOC obtained in the previous step or their initial values when $n=1$; a_i, b_i ($i=1,2,3$), β^*_{SOC}, and γ^* are the coefficients, which are defined as:

$$a_1=\begin{cases}\dfrac{TK_{Ud}}{T_{DC}} & |\Delta f(k)|>\mu_{fd}\\ 0 & |\Delta f(k)|\le\mu_{fd}\end{cases} \quad \text{(A13)}$$

$$a_2=\begin{cases}\dfrac{TK_{Ui}}{T_{DC}} & |F(k)|>\mu_F\\ 0 & |\Delta f(k)|\le\mu_F\end{cases} \quad \text{(A14)}$$

$$a_3=\begin{cases}-\dfrac{TK_\sigma K_f}{T_{DC}} & \Delta U_{dc}(k)>\mu_U\\ 0 & \Delta U_{dc}(k)\le\mu_U\end{cases} \quad \text{(A15)}$$

$$b_1=\begin{cases}-\dfrac{TK_{Ud}}{T_{DC}} & \Delta f(k)>\mu_{fd}\\ 0 & |\Delta f(k)|\le\mu_{fd}\\ \dfrac{TK_{Ud}}{T_{DC}} & \Delta f(k)<-\mu_{fd}\end{cases} \quad \text{(A16)}$$

$$b_2=\begin{cases}-\dfrac{TK_{Ui}}{T_{DC}} & F(k)>\mu_F\\ 0 & |F(k)|\le\mu_F\\ \dfrac{TK_{Ui}}{T_{DC}} & F(k)<-\mu_F\end{cases} \quad \text{(A17)}$$

$$b_3=\begin{cases}\dfrac{TK_\sigma K_f}{T_{DC}} & \Delta U_{dc}(k)>\mu_U\\ 0 & \Delta U_{dc}(k)\le\mu_U\end{cases} \quad \text{(A18)}$$

$$\beta^*_{\mathrm{SOC}}=\begin{cases}\dfrac{\mathrm{e}^{-k(SOC^*-SOC^{\mathrm{ch}})}}{1+\mathrm{e}^{-k(SOC^*-SOC^{\mathrm{ch}})}} & \text{charging mode}\\ \dfrac{\mathrm{e}^{k(SOC^*-SOC^{\mathrm{dis}})}}{1+\mathrm{e}^{k(SOC^*-SOC^{\mathrm{dis}})}} & \text{discharging mode}\end{cases} \quad \text{(A19)}$$

$$\gamma^*=\begin{cases}\dfrac{-k\mathrm{e}^{-k(SOC^*-SOC^{\mathrm{ch}})}}{(1+\mathrm{e}^{-k(SOC^*-SOC^{\mathrm{ch}})})^2}(K_{Bd}\Delta f^*+K_{Bi}F^*) & \text{charging mode}\\ \dfrac{k\mathrm{e}^{k(SOC^*-SOC^{\mathrm{dis}})}}{(1+\mathrm{e}^{k(SOC^*-SOC^{\mathrm{dis}})})^2}(K_{Bd}\Delta f^*+K_{Bi}F^*) & \text{discharging mode}\end{cases} \quad \text{(A20)}$$

Equations (A1)-(A12) can then be rewritten into the form of (25), where $\boldsymbol{x}(n)$ = $[\Delta f(n),\ F(n),\ \Delta P_V(n),\ \Delta P_G(n),\ \Delta P_{B0}(n),\ \Delta P_B(n),\ SOC(n);\ \Delta U_{dc}(n),\ \Delta P_{SE0}(n),\ \Delta P_{SE}(n),\ \Delta P_{WF0}(n),\ \Delta P_{WF}(n)]^{\mathrm{T}}$; $\boldsymbol{u}(n)=[\mu_{fd},\ \mu_F,\ \mu_U,\ \gamma^*\cdot SOC^*]^{\mathrm{T}}$; $\boldsymbol{r}(n)=[\Delta P_L]$; $\boldsymbol{y}(n)=[\Delta f(n),\ F(n),\ \Delta P_B(n),\ \Delta P_{SE}(n),\ \Delta P_{WF}(n),\ SOC(n)]^{\mathrm{T}}$; $\boldsymbol{A}$ is a 12×12-order state matrix; $\boldsymbol{B}$ is a 12×4-order input matrix; $\boldsymbol{R}$ is a 12×1-order disturbance matrix; and $\boldsymbol{C}$ is a 6×12-order output matrix.

APPENDIX B

In the system, the base power, base AC voltage, and base DC voltage are 400 MVA, 220 kV, and 400 kV, respectively.

TABLE BI
PARAMETERS OF AC1

Symbol	Item	Value
S_G	Rated generator power	2.0 p.u.
U_G	Rated terminal voltage	1.0 p.u.
H_G	Inertia time constant	6 s
K_G	Droop coefficient of generator	40
T_G, T_{CH}	Governor and turbine time constants	0.08 s, 0.2 s
P_G	Initial generator power output	1.4 p.u.
P_L	Initial load (with 20% dynamic load)	2.3 p.u.
$P_{B\max 0}$	Nominal maximum power of BESS	0.2 p.u.
SOC_0	Initial SOC of BESS (in cases 1 and 3)	50%
E_B	BESS capacity	100 MWh

TABLE BII
PARAMETERS OF SYSTEM FRM

Symbol	Item	Value
J_s, D_s	System equivalent inertia and damping	32 s, 4
T_1	Power response time constant of BAMMC	0.01 s
T_2	Power response time constant of SELCC	0.01 s
T_3	Power response time constant of WFMMC	0.01 s
T_B	Power response time constant of BESS	0.02 s
T_{LCC}	Power response time constant of AC2	0.02 s
T_{WF}	Power response time constant of WF	0.1 s
T_{DC}	DC voltage response time constant of REMMC	0.01 s

TABLE BIII
PARAMETERS OF OPTIMIZATION MODEL

Symbol	Item	Value
c_{f1}, c_{f2}, c_{f3}	Weight coefficients in M_f	2.1, 2.1, 2.1
c_{P1}, c_{P2}, c_{P3}	Weight coefficients of M_P	1, 1, 1.5
$K_{Bi\min}$, $K_{Bi\max}$	Lower and upper bounds of K_{Bi}	1, 10
$K_{Bd\min}$, $K_{Bd\max}$	Lower and upper bounds of K_{Bd}	2, 20
$K_{P\min}$, $K_{P\max}$	Lower and upper bounds of K_P	2, 20

TABLE BIV
PARAMETERS OF CONVERTERS AND HVDC LINK

Symbol	Item	Value
S_{MMC}	Rated MMC power	1.0 p.u.
U_{MMC}	Rated MMC AC root mean square (RMS) voltage	0.909 p.u.
S_{LCC}	Rated LCC power	1.0 p.u.
U_{LCC}	Rated LCC AC RMS voltage	0.909 p.u.
S_{dc}	Rated DC power	1.0 p.u.
U_{dc0}	Rated DC voltage	1.0 p.u.
f_0	Rated system frequency	50 Hz
N_{sm}	Number of submodules	200
C_{sm}	Capacitance in submodules	10 mF
L_{arm}, R_{arm}	Bridge arm inductance and resistance	0.5 p.u., 0.005 p.u
L_T, R_T	Transformer inductance and resistance	0.1 p.u., 0.005 p.u.
L_l, R_l	Cable inductance and resistance	0.05 p.u., 0.005 p.u.

TABLE BV
PARAMETERS OF AC2

Symbol	Item	Value
S_G	Rated generator power	4.0 p.u.
U_G	Rated terminal voltage	1.0 p.u.
H_G	Inertia time constant	8 s
K_G	Droop coefficient of generator	40
T_G, T_{CH}	Governor and turbine time constants	0.08 s, 0.2 s
P_G	Initial generator power output	3.6 p.u.
P_L	Initial load	3.2 p.u.
P_{SE0}	Initial power reference of SELCC	0.4 p.u.
P_{res}	Power reserve of AC2	0.4 p.u.
η	Ratio for supporting other networks	50%

TABLE BVI
PARAMETERS OF WF

Symbol	Item	Value
S_n	Rated DFIG power	2.778×10^{-3} p.u.
P_n	Rated active power	2.5×10^{-3} p.u.
N_{wt}	Number of DFIGs	200
f_{WF0}	Rated WF frequency	50 Hz
v_n	Rated wind speed	12 m/s
H_{WT}	Inertia time constant	4.32 s
σ_m	The maximum power reduction ratio	20%

REFERENCES

[1] Y. Li, L. Luo, C. Rehtanz *et al.*, "Realization of reactive power compensation near the LCC-HVDC converter bridges by means of an inductive filtering method," *IEEE Transactions on Power Electronics*, vol. 27, no. 9, pp. 3908-3923, Sept. 2012.

[2] M. Li, Z. Guo, D. Cai *et al.*, "Operating characteristic analysis of multi-terminal hybrid HVDC transmission system with different control strategies," in *Proceedings of 2018 International Conference on Power System Technology*, Guangzhou, China, Nov. 2018, pp. 2616-2621.

[3] L. Yang, Y. Li, Z. Li *et al.*, "A simplified analytical calculation model of average power loss for modular multilevel converter," *IEEE Transactions on Industrial Electronics*, vol. 66, no. 3, pp. 2313-2322, Mar. 2019.

[4] G. S. Lee, D. H. Kwon, and S. I. Moon, "Method for determining the droop coefficients of hybrid multi-terminal HVDC systems to suppress AC voltage fluctuations," *IEEE Transactions on Power Systems*, vol. 35, no. 6, pp. 4944-4947, Nov. 2020.

[5] J. Li, B. Zhu, Y. Guo *et al.*, "The simulation of Kunliulong flexible DC project with single station operation and out of operation," in *Proceedings of 2021 IEEE/IAS Industrial and Commercial Power System Asia*, Chengdu, China, Jul. 2021, pp. 1028-1034.

[6] A. Oudalov, D. Chartouni, and C. Ohler, "Optimizing a battery energy storage system for primary frequency control," *IEEE Transactions on Power Systems*, vol. 22, no. 3, pp. 1259-1266, Aug. 2007.

[7] I. Serban and C. Marinescu, "Control strategy of three-phase battery energy storage systems for frequency support in microgrids and with uninterrupted supply of local loads," *IEEE Transactions on Power Electronics*, vol. 29, no. 9, pp. 5010-5020, Sept. 2014.

[8] A. Moeini, I. Kamwa, Z. Gallehdari *et al.*, "Optimal robust primary frequency response control for battery energy storage systems," in *Proceedings of 2019 IEEE PES General Meeting*, Atlanta, USA, Aug. 2019, pp. 1-5.

[9] T. Zhao, A. Parisio, and J. V. Milanović, "Distributed control of battery energy storage systems for improved frequency regulation," *IEEE Transactions on Power Systems*, vol. 35, no. 5, pp. 3729-3738, Sept. 2020.

[10] G. Meng, Q. Chang, Y. Sun *et al.*, "Energy storage auxiliary frequency modulation control strategy considering ACE and SOC of energy storage," *IEEE Access*, vol. 9, pp. 26271-26277, Feb. 2021.

[11] L. M. Castro and E. Acha, "On the provision of frequency regulation in low inertia AC grids using HVDC systems," *IEEE Transactions on Smart Grid*, vol. 7, no. 6, pp. 2680-2690, Nov. 2016.

[12] H. Liu and Z. Chen, "Contribution of VSC-HVDC to frequency regulation of power systems with offshore wind generation," *IEEE Transactions on Energy Conversion*, vol. 30, no. 3, pp. 918-926, Sept. 2015.

[13] M. Guan, J. Cheng, C. Wang *et al.*, "The frequency regulation scheme of interconnected grids with VSC-HVDC links," *IEEE Transactions on Power Systems*, vol. 32, no. 2, pp. 864-872, Mar. 2017.

[14] Y. Phulpin, "Communication-free inertia and frequency control for wind generators connected by an HVDC-link," *IEEE Transactions on Power Systems*, vol. 27, no. 2, pp. 1136-1137, May 2012.

[15] Y. Li, Z. Zhang, Y. Yang *et al.*, "Coordinated control of wind farm and VSC-HVDC system using capacitor energy and kinetic energy to improve inertia level of power systems," *International Journal of Electrical Power & Energy Systems*, vol. 59, pp. 79-92, Mar. 2014.

[16] Z. Ma, X. Wang, S. Wu *et al.*, "Coordinated control strategy of offshore wind farm and MMC-HVDC to improve the inertia level of power system," in *Proceedings of 2019 IEEE 8th International Conference on Advanced Power System Automation and Protection*, Xi'an, China, Oct. 2019, pp. 1819-1823.

[17] J. Chu, Y. Lv, Y. Xu *et al.*, "Coordinated control strategy for improving frequency stability of offshore wind farms connected to the grid through MMC-HVDC transmission," in *Proceedings of the 4th Asia Energy and Electrical Engineering Symposium*, Chengdu, China, Mar. 2022, pp. 354-360.

[18] J. Rafferty, L. Xu, W. Yi *et al.*, "Frequency support using multi-terminal HVDC systems based on DC voltage manipulation," *IET Renewable Power Generation*, vol. 10, no. 9, pp. 1393-1401, Jul. 2017.

[19] G.-S. Lee, D.-H. Kwon, S.-I. Moon *et al.*, "A coordinated control strategy for LCC HVDC systems for frequency support with suppression of AC voltage fluctuations," *IEEE Transactions on Power Systems*, vol. 35, no. 4, pp. 2804-2815, Jul. 2020.

[20] C. Guo, P. Cui, and C. Zhao, "Optimization and configuration of control parameters to enhance small-signal stability of hybrid LCC-MMC HVDC system," *Journal of Modern Power Systems and Clean Energy,* vol. 10, no. 1, pp. 213-221, Jan. 2022.

[21] Q. Zhang, J. D. McCalley, V. Ajjarapu *et al.*, "Primary frequency support through North American continental HVDC interconnections with VSC-MTDC systems," *IEEE Transactions on Power Systems*, vol. 36, no. 1, pp. 806-817, Jan. 2021.

[22] Ministry of Power Industry of the People's Republic of China. (1996, Oct.). Rules for power supply. [Online]. Available: http://www.nea.gov.cn/2012-01/04/c_131262676.htm

[23] T. Baškarad, N. Holjevac, I. Kuzle *et al.*, "ROCOF importance in electric power systems with high renewables share: a simulation case for Croatia," in *Proceedings of the 12th Mediterranean Conference on Power Generation, Transmission, Distribution and Energy Conversion*, Online Conference, Sept. 2020.

[24] Standardization Administration of the People's Republic of China.

(2021, Aug.). Technical specification for connecting wind farm to power system – Part 1. [Online]. Available: http://c.gb688.cn/bzgk/gb/showGb?type=online&hcno=F0127C2B431AC283CD6ED17CE67F8E46

[25] A. Raza, Z. Yousaf, M. Jamil *et al.*, "Multi-objective optimization of VSC stations in multi-terminal VSC-HVDC grids based on PSO," *IEEE Access*, vol. 6, pp. 62995-63004, Oct. 2018.

[26] C. Guo, Z. Yin, Y. Wang *et al.*, "Investigation on small-signal stability of hybrid LCC-MMC HVDC system," *Proceedings of the CSEE*, vol. 39, no. 4, pp. 1040-1052, Feb. 2019.

[27] Y. Mu, J. Wu, J. Ekanayake *et al.*, "Primary frequency response from electric vehicles in the Great Britain power system," *IEEE Transactions on Smart Grid*, vol. 4, no. 2, pp. 1142-1150, Jun. 2013.

[28] D. Pattabiraman, R. H. Lasseter, and T. M. Jahns, "Comparison of grid following and grid forming control for a high inverter penetration power system," in *Proceedings of 2018 IEEE PES General Meeting (PESGM)*, Portland, USA, Aug. 2018, pp. 1-5.

Jialiang Wu received the B.Eng. degree in electrical engineering from Zhejiang University, Hangzhou, China, in 2018, where he is currently pursuing the Ph. D. degree in electrical engineering. His research interests include power system frequency stability analysis and control of renewable energy and voltage-source converter based high-voltage direct current (VSC-HVDC) transmission.

Zhen Wang received the B.Eng., M.Eng., and Ph.D. degrees from Xi'an Jiaotong University, Xi'an, China, Zhejiang University, Hangzhou, China, and Hong Kong Polytechnic University, Hong Kong, China, in 1998, 2001, and 2009, respectively. He is currently a Full-time Professor and the Director of Institute of Power and Energy Integration & Intelligence, Zhejiang University. He was the recipient of 2014 Endeavour Research Fellowship sponsored by Australia Government and Visiting Scholar of The University of Western Australia, Perth, Australia. He is an expert member of IEC TC8/SC8B/JWG1 Working Group on Microgrid Operation and Control. He also serves as the editor of the journal Electronics, and the member of some topical advisory panel. His research interests include power system stability and control, renewable energy integration, and VSC-HVDC transmission.

Ruixu Liu received the B.Eng. degree in electrical engineering from Southwest Jiaotong University, Chengdu, China, in 2019. She is currently pursuing the Ph.D. degree in electrical engineering in Zhejiang University, Hangzhou, China. Her research interests include control and stability analysis of power-electronics-based power systems.

Yu Shan received the B. Eng. degree in electrical engineering from Southwest Jiaotong University, Chengdu, China, in 2020. He is currently pursuing the Ph.D. degree in electrical engineering in Zhejiang University, Hangzhou, China. His research interests include power system frequency stability analysis and control of power-electronics-based devices.

Chenxuan Wang received the B. Eng. and Ph. D. degrees from the College of Electrical Engineering, Zhejiang University, Hangzhou, China, in 2017 and 2022, respectively. He was a Visiting Student at Technical University of Denmark, Copenhagen, Denmark, from Sept. 2019 to Sept. 2020. He is currently working at the Economic Research Institute of State Grid Zhejiang Electric Power Co., Ltd., Hangzhou, China. His research interests include the power system electromagnetic transient simulation, frequency dependent network equivalent, and sub-synchronous oscillation analysis of grid-connected wind farms.